Sustainable dual usage of spray pyrolyzed SnO_2:Sb thin film: Pollutant degradation and power generation

Gouranga Maharana[1], Yuvashree J[1], Sudipa Bhadra[2], Soubhagya Nayak[2], Surajbhan Sevda[2], D. Paul Joseph[1*], Hari Prasad Kokatla[3] Manavalan Kovendhan[4]

[1]Department of Physics, National Institute of Technology, Warangal, Telangana State-506004, India.
[2]Department of Biotechnology, National Institute of Technology, Warangal, Telangana State-506004, India.
[3]Department of Chemistry, National Institute of Technology, Warangal, Telangana State-506004, India.
[4]Department of Physics and Nanotechnology, SRM Institute of Science and Technology, Kattankulathur, Tamilnadu-603203, India.

*Corresponding author e-mail: paul@nitw.ac.in

S1. The visible light spectrum of 200 W LED

To achieve photocatalytic activity through a defect-mediated mechanism of SnO_2 films, white visible light is used for the test. The figure below represents the light spectrum of the used 200 W LED light in order to understand the light intensity received by the SnO_2 photoelectrodes to carry out the photocatalytic tests. This spectrum clearly shows that the white light emitted by the LED consists of visible region wavelengths with two major peaks around 450 and 530 nm, respectively.

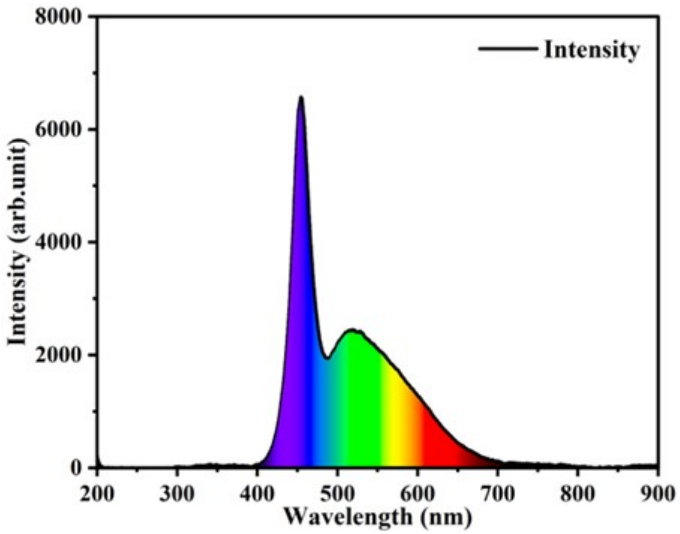

Figure S1. The visible light spectrum of the 200 W LED light used for the photocatalytic study showing sharp peak intensity around 450 nm and a broad peak at 530 nm

S2. Williamson-Hall plots

The lattice stress within the deposited films was quantified using the Williamson-Hall equations [1]. The positive slope of the W-H plot (Fig. S2) implies that the spray-coated films have a tensile stress (ε).

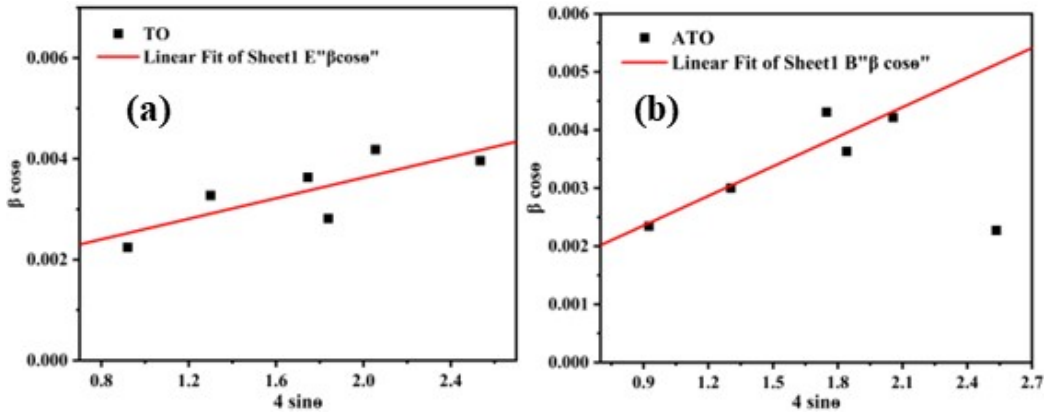

Figure S2: Williamson-Hall plots for (a) TO and (b) ATO films

S3. Elemental Mapping and EDAX measurements

The elemental mapping representation shows that the Sn, O, and Sb elemental constituents are nearly consistently disseminated throughout the area with no substantial aggregation (Figs. S3a-c, and g-j). Figures S3(d-e and k-l) show the tentative stoichiometric ratio of constituent elements of the pure and Sb-doped SnO_2 film corresponding to Sn, Sb, and O based on EDAX measurements. The modest discrepancy in Sb dopant element content from the required value could be attributed to subtle fluctuations in spray dynamics.

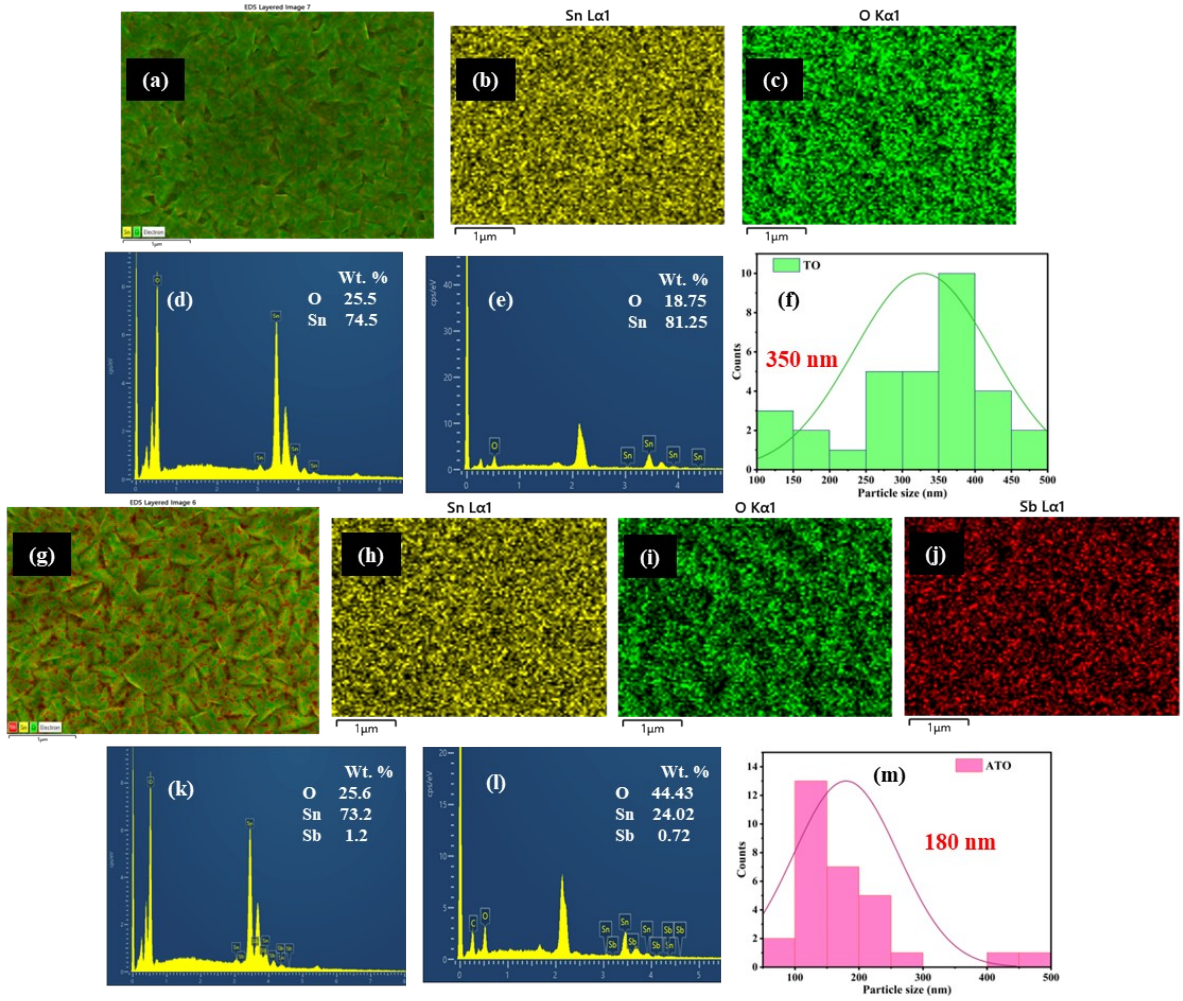

Figure S3. Elemental mapping, EDAX measurements and particle size distribution of TO (a-f) and ATO (g-m) films, respectively.

The open-source Image J (Version 1.53t) software is used to estimate the size distribution of tetragonal-like structures. Figure (S3f and m) depict the particle size distribution of all the deposited films, and Sb doping into the SnO_2 lattice causes the average grain size to drop significantly. The insertion of Sb dopant into the SnO_2 lattice resulted in the average particle size decreasing from 350 to 180 nm. The addition of Sb induces the particles to become sharper and more randomly oriented, which may result in greater light scattering, impacting the transmittance of the films. Coupling these findings to preceding knowledge regarding polycrystalline films, it is widely documented that growth factors, like substrate temperature,

precursor concentration and solution volume, have significant effects on the film's morphological and structural features.

S4. Surface topography

The surface topographical features of nanoscale semiconductors play an important role in defining their physicochemical and optoelectronic applications. The optical profilometer is effective for quantitatively measuring the dimensional surface roughness over a large region (1 mm × 1 mm) and visualising the surface nano-texture of the deposited film in a non-contact method of operation (Fig. S4). Optical profilers employ reflections of light to detect topological details along a line or area. The surface of the pristine SnO_2 film exhibits aggregation of grains with non-uniform granular dimensions. The incorporation of Sb dopant into the SnO_2 lattice leads to a significant improvement in grain size uniformity. Gwyddion (Version 2.61) software was employed to acquire the RMS surface roughness (r_w) of the spray deposited films [2]. The corresponding cross-sectional roughness profiles obtained from the Gwyddion software for TO and ATO are depicted in Figs. S4a and S4b, respectively. The larger-sized particles of the TO sample are shown in Figs. 4a and S3f are commensurate with its higher surface roughness. The increasing surface roughness (r_w) value of the TO film also aids towards its thickness. ATO film's lower surface roughness can be attributed to the smaller and substantially smoother particles on the film's surface (Figs. 4f and S3m). The insertion of the Sb dopant is the key factor behind the surface roughness variation, which is modulated by the film's nucleation and growth mechanism. Multiple factors influence the nucleation and growth process of thin films, involving substrate temperature, coating rate, ionic states and energies, dopant type, and other related parameters. Multiple nucleation taking place during the coating process, leading to a granular feature, resulting in the fluctuation of the film thickness. In order to minimize discrepancy, the thickness values stated are the average of every film measured at several sites using a stylus profiler. Subsequently, the thickness estimated from the FESEM cross-sectional

images (Figs. 4c and h) is analysed alongside the data received from the stylus profilometer (Table 1); both techniques yield almost equivalent values with minor deviations. Furthermore, the cross-sectional images vividly demonstrate the creation of a layer upon the glass substrate. The film thickness is governed by a variety of parameters, including subtle deviations in the dynamics of spray-like aerosol time of flight, pressure, droplet size, rate of coating, temperature gradient, and so on.

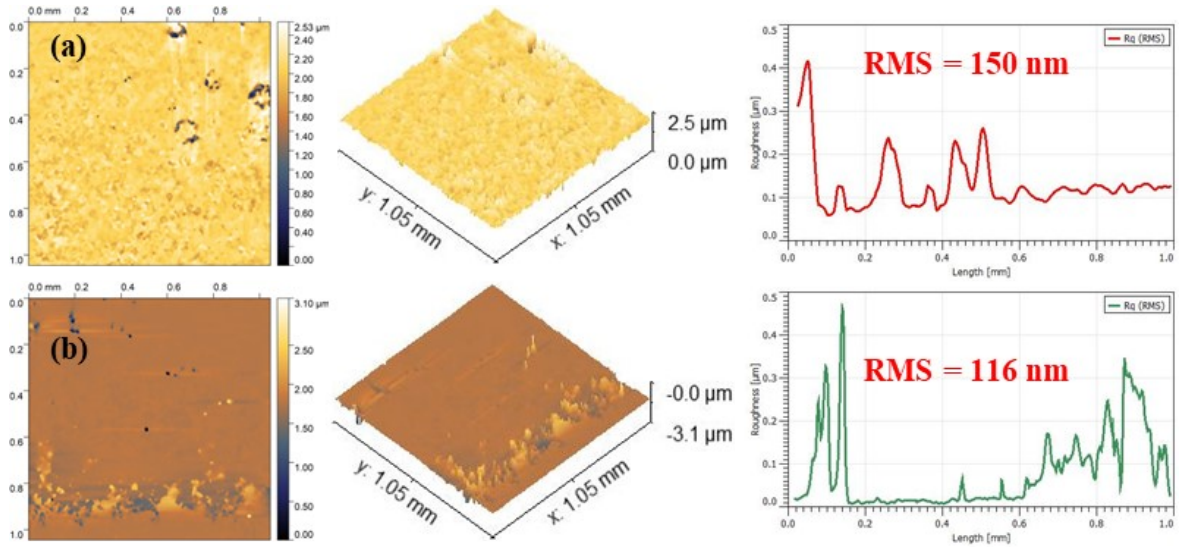

Figure S4. Optical profiler images (2D and 3D) alongside their corresponding cross-sectional roughness profile of (a) TO and (b) ATO, samples respectively

S5. Four-probe measurements

The sheet resistance R_s is calculated using Eq. (S1) by determining the voltage (V) between the two inner contacts and the current (I) applied between the two outer contacts.

$$R_s = 4.532 \times \frac{V}{I} \qquad (S1)$$

The thickness of the film is considerably smaller than the spacing between the probes (≅1 mm), hence a correction factor of 4.532 is utilised, with V and I representing the voltage and applied current, respectively. The assessed sheet resistance from the linear four-probe in comparison to the values from the Hall effect establishes that both approaches follow similar behaviour with only a minor variation, confirming the electrical uniformity of the spray pyrolyzed pure and Sb-doped SnO_2 thin film samples.

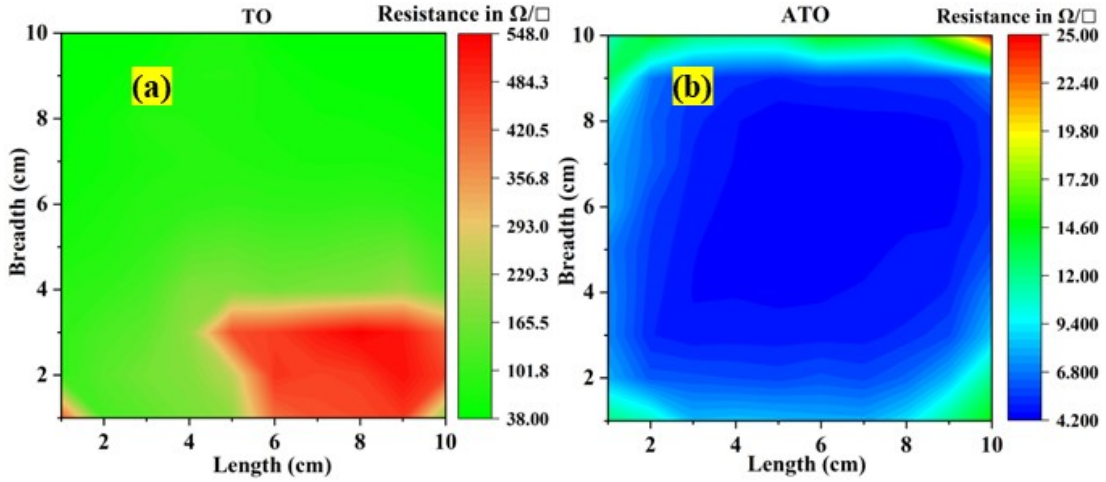

Figure S5. 2D contour mapping of sheet resistance (a- TO, b-ATO) estimated by the linear four-probe method over 10 × 10 cm^2 of the spray-coated films, showing variance in sheet resistance across the substrate

S6. Absorption spectra of degrading methylene blue dye under varying light irradiation

The photocatalytic activity of the deposited pure and 5 wt.% Sb: SnO_2 films are assessed via monitoring the shift in optical absorption of the MB dye at 664 nm during its photocatalytic degradation process. The UV-Vis absorbance spectra (for photolysis, TO and ATO catalysts) obtained at different illumination periods are displayed in the figures and are used for estimating the kinetics of this process.

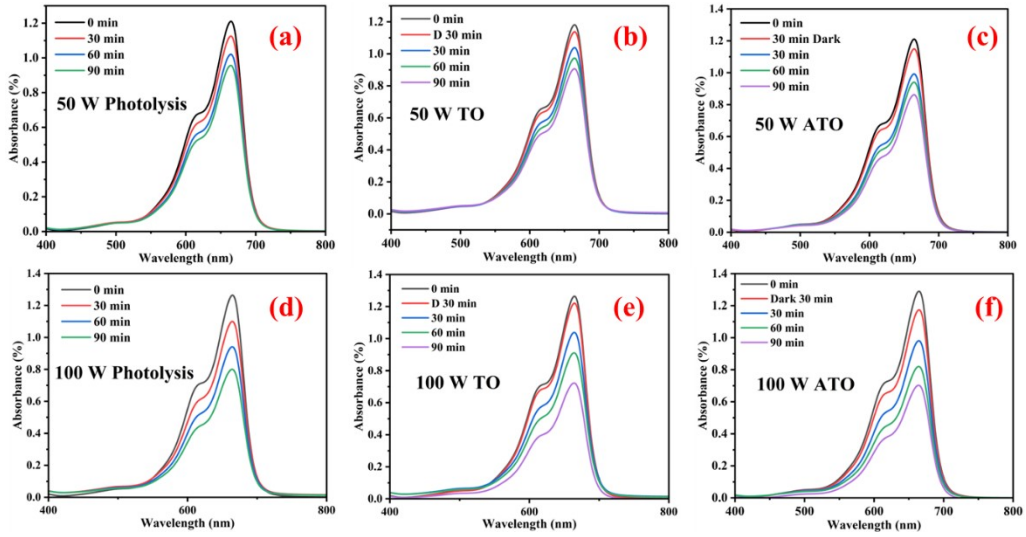

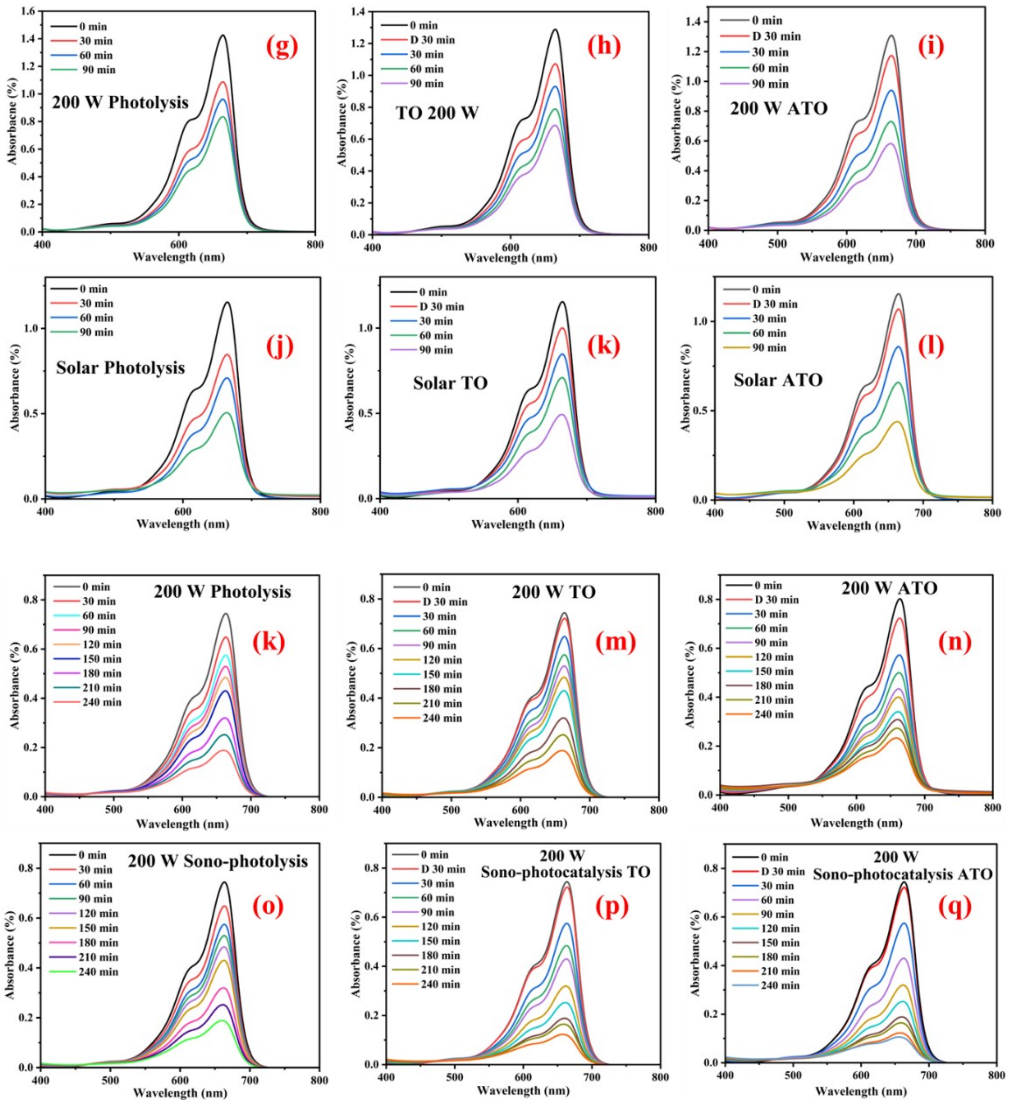

Figure S6. Absorbance spectra of MB dye degradation under various conditions (a) 50 W photolysis, (b) 50 W TO photocatalysis, (c) 50 W ATO photocatalysis, (d) 100 W photolysis, (e) 100 W TO photocatalysis, (f) 100 W ATO photocatalysis, (g) 200 W photolysis, (h) 200 W TO photocatalysis, (i) 200 W ATO photocatalysis, (j) Solar photolysis, (k) Solar TO photocatalysis, (l) Solar ATO photocatalysis, (k) 200 W photolysis (240 min), (m) 200 W TO photocatalysis (240 min), (n) 200 W ATO photocatalysis (240 min), (o) 200 W Sono-photolysis (240 min), (p) 200 W TO Sono-photocatalysis (240 min) and (q) 200 W ATO Sono-photocatalysis (240 min)

S7. EDS Spectra of the used ATO film for degradation of MB dye

The EDS measurement was used to analyse the elemental composition of the degraded pollutants on the surface of the ATO electrode following the photodegradation of the MB dye. The EDS plot shows the presence of constituent elements of the MB dye as C, N, S and Cl on

the photoelectrode's surface. The At.% composition of the constituent elements is shown in Table S1.

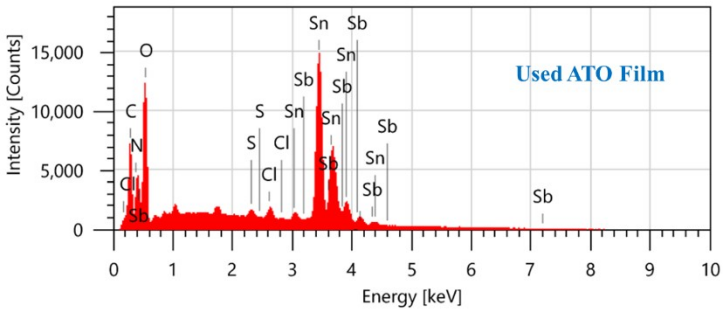

Figure S7. EDS measurement of the used ATO film after the photodegradation of MB dye

Table S1. EDS measurement of the used ATO film after the photodegradation of MB dye.

Elements	At. % of constituent elements
C	13.43
N	10.60
O	51.36
S	0.67
Cl	1.05
Sn	22.67
Sb	0.21
Total	100

S8. Total organic carbon (TOC)

The MB dye (after 240 min of sono-photocatalysis) was also analysed for quantitative mineralization dependent on the total organic carbon (TOC) removal percentage. The TOC analysis was acquired using a TOC analyser (TOC-L CPN, SHIMADZU) prior to and following the photodegradation of the MB dye. The TOC removal effectiveness was computed as:

$$TOC\ removal\ (\%) = \frac{TOC_i - TOC_f}{TOC_i} \times 100 \qquad (S2)$$

where TOC_i and TOC_f represent the total organic carbon content (mg/L) of the MB dye preceding and following photocatalysis, respectively. A moderate drop in TOC was observed,

indicating successful mineralisation of MB with ATO film. The TOC reduced from 8 to 5.3 mg/L, representing a 33.7 % elimination of the MB dye. However, TOC removal serves the purpose of determining the mineralisation rate. The TOC measurements do not represent the overall TOC concentration because of the loss of volatile chemicals (i.e., acetaldehyde, formaldehyde) inside the gaseous stream following ozonation. Exact mass ratio and mineralisation rate calculations cannot be made solely on the reported results; the tendencies of the estimated parameters during the treatment process are useful in assessing ozonation efficiency [3].

S9. Behaviour of power density with respect to current density

Behaviour of the areal power density in relation to current density (power density vs current density in OCV mode) for the as-deposited electrodes in the dual-chamber MFC was measured and shown in Figs. S8a and b for TO and ATO, respectively. The external resistance versus power density curve and the volumetric power density curve exhibit entirely distinct sorts of trend when the external resistance is varied from 10,000 to 10 Ω. The microorganisms eventually used the organic substrate since the MFCs were operating without adding glucose, and as a result, a reduction in cell voltage, current density, power density, and volumetric power density production was observed [4,5].

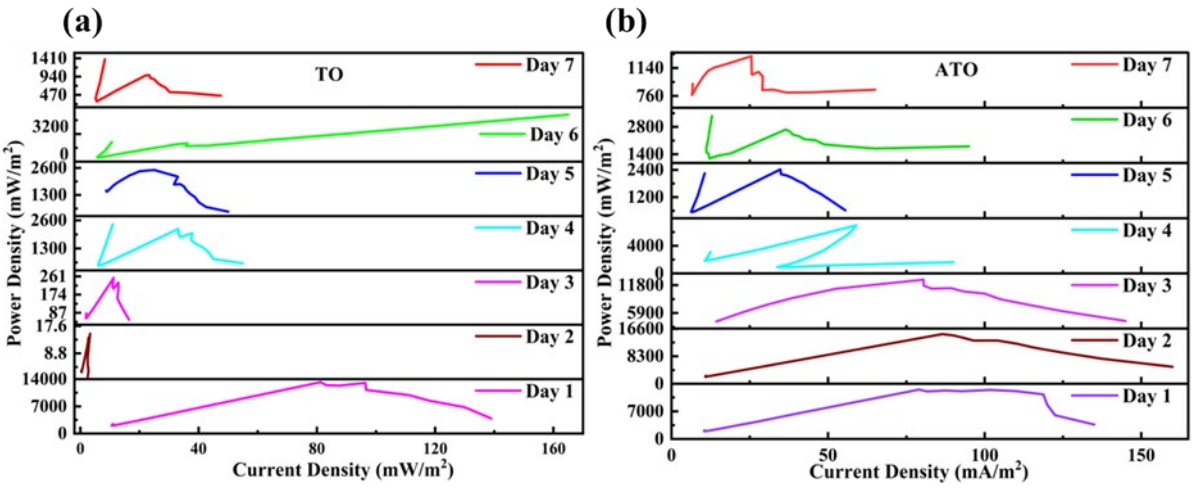

Figure S8. Behaviour of power density with respect to current density for (a) TO and (b) ATO cathodic electrodes in the dual-chamber MFC

S10. EDS Spectra of the used TO and ATO film for MFC

The EDS measurement was used to analyse the elemental composition of the biofilm formed on the biocathode surface following the MFC usage. The EDS plot shows the presence of constituent elements of the formed biofilms as C, Na, Mg, P, S, Cl, K, Ca, Cu and Zn on the biocathode's surface.

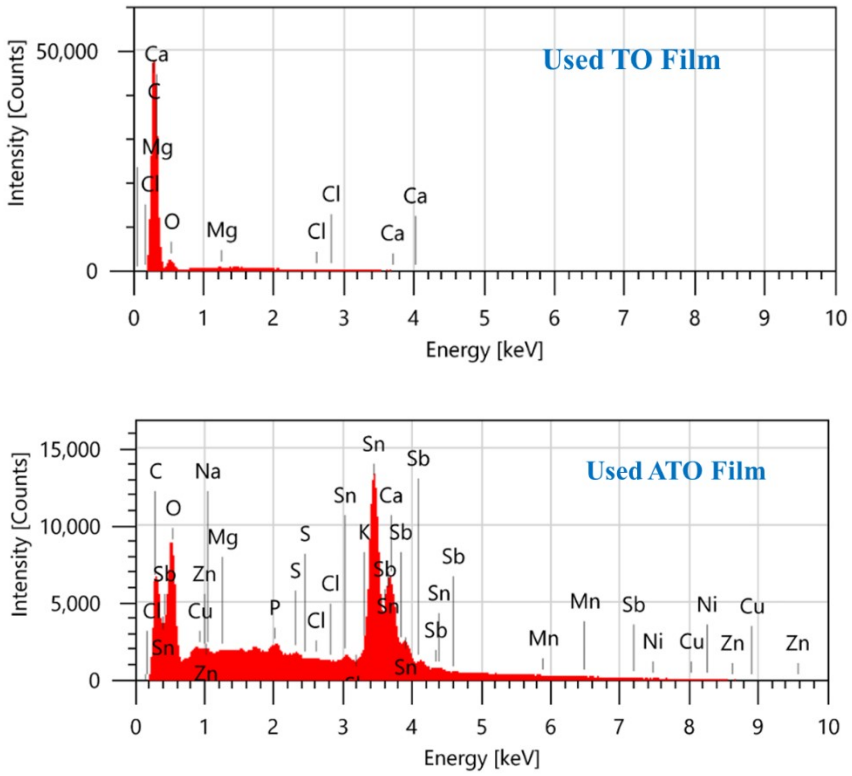

Figure S9. EDS measurement of the biocathodes used in the MFC's cathodic chamber.

Table S2. Elemental composition obtained from EDS measurements of the biocathodes used in the MFC's cathodic chamber.

Elements	At. % of constituent elements	
	TO Film	ATO Film
C	18.29	14.58
O	51.68	56.98
Na	--	0.40
Mg	0.02	0.17
P	--	1.10
S	--	0.36
Cl	0.01	0.10

K	--	0.22
Ca	0.01	0.09
Cu	--	0.75
Zn	--	0.40
Sn	29.99	23.86
Sb	--	1
Total	100	100

[1] V.S. Vinila, J. Isac, Synthesis and structural studies of superconducting perovskite GdBa2Ca3Cu4O10.5+δ nanosystems, Des. Fabr. Charact. Multifunct. Nanomater. (2022) 319–341. https://doi.org/10.1016/B978-0-12-820558-7.00022-4.

[2] L.M. Ward, R.M. Shah, J.D. Schiffman, S.T. Weinman, Nanopatterning Reduces Bacteria Fouling in Ultrafiltration, (2022). https://doi.org/10.1021/acsestwater.2c00256.

[3] A.R. Tehrani-Bagha, N.M. Mahmoodi, F.M. Menger, Degradation of a persistent organic dye from colored textile wastewater by ozonation, Desalination. 260 (2010) 34–38. https://doi.org/10.1016/J.DESAL.2010.05.004.

[4] S. Bhadra, S. Nayak, S. Sevda, Simultaneous organic wastewater treatment and bioelectricity production in a dual chamber microbial fuel cell with Scenedesmus obliquus biocathode, Energy Convers. Manag. 316 (2024) 118849. https://doi.org/10.1016/J.ENCONMAN.2024.118849.

[5] A. Bindu, S. Bhadra, S. Nayak, R. Khan, A.A. Prabhu, S. Sevda, Bioelectrochemical biosensors for water quality assessment and wastewater monitoring, Open Life Sci. 19 (2024). https://doi.org/10.1515/BIOL-2022-0933/ASSET/GRAPHIC/J_BIOL-2022-0933_FIG_003.JPG.

****